Materials Advances

ROYAL SOCIETY OF CHEMISTRY

PAPER

View Article Online
View Journal | View Issue

Cite this: *Mater. Adv.*, 2024, 5, 3014

A MnS/MnO-coated S,N-doped carbon anode obtained from a Mn(II)-coordinated polymer for long-cycle life Li-ion batteries†

Kyubin Shim, ‡[a] Hyun Woo Kim,‡[a] Sungwoo Park,[a] Kyeong-Deok Seo,[b] Chang-Yeon Kim, [a] Jin Bae Lee,[a] Jong Seong Bae[c] and Hae Jin Kim*[a]

Received 23rd January 2024,
Accepted 17th February 2024

DOI: 10.1039/d4ma00066h

rsc.li/materials-advances

To address the limitations of the anodes used in current Li-ion batteries (LIBs), a MnS/MnO-decorated S,N-doped carbon (MSNC) electrode was designed by introducing a Mn^{2+}-coordinated polymer (Mn-DTOGA) bonded to a sulfur atom with acetate counter ions through an imine formation reaction for advanced LIBs. The MSNC electrode was prepared and characterized by X-ray photoelectron spectroscopy (XPS), X-ray diffraction (XRD), scanning electron microscopy, and transmission electron microscopy, which confirmed the ease of synthesis, superior controllability, and uniformity of the material. The electrochemical characteristics of the materials were assessed *via* cyclic voltammetry, electrochemical impedance spectroscopy, and galvanostatic charge–discharge tests to determine their viability as anode materials in LIBs. The results demonstrate excellent cycling stability, with the material exhibiting superior performance for 500 cycles at a rate of 0.2 C. Furthermore, *in situ* XRD and XPS measurements provided a fundamental understanding of the material, confirming the redox reaction between the MnS/MnO complex and metallic Mn/Li_2S/Li_2O.

Introduction

Li-ion batteries (LIBs) are the main technologies used in the electric vehicle and power storage industries.[1–3] Currently, the energy density of LIBs is reaching its limit.[4,5] This is mainly because of the low specific capacity (approximately 372 mA h g^{-1}) of commercially available graphite-based negative electrodes.[6,7] Thus, there is strong motivation to investigate high-performance anode materials because of the rapidly increasing demand for LIBs.[8,9]

In the last few decades, transition metal oxides (756 mA h g^{-1}) and transition metal sulfides (616 mA h g^{-1}) have been proposed as alternatives to carbon-based materials because of their high theoretical specific capacities resulting from the conversion processes.[10–14] Mn-based materials, such as MnO and α-MnS, are regarded as desirable alternative anodes for LIBs, owing to their advantages, such as environmental friendliness, natural abundance, and low operating potentials.[15,16] However, during repeated charge–discharge cycles, Mn-based compounds with high capacities experience several issues. In particular, a short cycle lifespan is caused by substantial structural changes during delithiation, and a poor rate capability is caused by low electrical conductivity and slow kinetics, which restrict their practical applications.[17]

Several methods have been suggested to address these issues and achieve a good Li storage performance. Embedding nanosized MnO or MnS into a carbon matrix can shorten the Li-ion diffusion pathway, reduce the volume change during repeated charging and discharging, and enhance electronic conductivity. In particular, the enhanced Li affinity and customized electrical structures of heteroatom-doped carbons make them ideal candidates for rapid Li^+/electron transport.[18,19]

Recently, it has been shown that oxide/sulfide heterostructures, created using oxide and sulfide semiconductors with various bandgaps, can generate an internal electric field at the interfaces to accelerate the transport of ions and electrons, and are potential candidates for Li/Na-ion storage.[20,21] Additionally, compared to sulfides, oxides provide a larger specific capacity for the same metal but poorer conductivity and more severe polarization during the charge–discharge process. Consequently, oxide/sulfide heterostructures can fully exploit the advantages of each material. Embedding oxide/sulfide heterostructures into a carbon matrix is a practical technique for achieving high-performance Li storage. For example, porous N,S-*co*-doped carbon-embedded MnO/MnS heterostructures developed by Zhang *et al.* demonstrated a high specific capacity

[a] *Research Center for Materials Analysis, Korea Basic Science Institute, Daejeon 34133, Republic of Korea. E-mail: hansol@kbsi.re.kr*
[b] *Department of Chemistry and Chemistry Institute for Functional Materials, Pusan National University, Busan 46241, Republic of Korea*
[c] *Busan Center, Korea Basic Science Institute, Busan 46742, Republic of Korea*

† Electronic supplementary information (ESI) available. See DOI: https://doi.org/10.1039/d4ma00066h

‡ The first two authors contributed to the work equally.

of 591 mA h g^{-1} at 0.1 A g^{-1} and significant cycling performance.[20] Chen *et al.* reported the synthesis of N and S co-doped carbon-confined MnO/MnS heterostructures derived from the one-step pyrolysis of Mn-methionine frameworks. When used as an anode material, these heterostructures exhibited capacities of 574/577 mA h g^{-1} at 0.5 A g^{-1}.[22] Nevertheless, the fabrication of composites with a wide range of properties typically requires labor-intensive and expensive syntheses, which are challenging to scale-up for practical applications. Furthermore, the production of well-defined oxide/sulfide heterostructures with carbon matrices remains challenging. Consequently, it is essential to develop a straightforward and efficient technique for reducing the complexity of the synthesis process.[20–22] Given these aspects, we recently reported MnS/MnO-decorated N,S-doped carbon derived from an Mn(II)-coordinated polymer, providing a new synthesis method and high electrochemical performance.[23]

In this study, we synthesized a Mn^{2+}-coordinated polymer bonded to a sulfur atom with acetate counter ions (Mn-DTOGA) *via* an imine formation reaction. Subsequently, the Mn ion-coordinated polymer was calcinated at 1000 °C to obtain homogeneous MnS/MnO-decorated S,N-doped carbon (herein, MSNC) nanoparticles for practical applications. The exceptional chemical and physical properties of the MSNC nanoparticles were thoroughly characterized using X-ray photoelectron spectroscopy (XPS), X-ray diffraction (XRD), scanning electron microscopy (SEM), and transmission electron microscopy (TEM). To assess their suitability as anode materials in LIBs, the electrochemical properties of the MSNC materials were evaluated using electrochemical impedance spectroscopy (EIS), cyclic voltammetry (CV), and galvanostatic charge–discharge tests. In addition, *in situ* XRD and XPS analyses were performed. The results provide strong evidence that MSNC holds great promise for the development of high-energy-density LIBs, owing to their superior chemical, physical, and electrochemical properties.

Experimental

Materials and reagents

Dithiooxamide (DTO, 97%), Mn(II) acetate tetrahydrate ($Mn(OAc)_2{\cdot}4H_2O$, 99.99% trace metal basis), polyvinylpyrrolidone (PVP; average $M_w \approx 29\,000$), glutaraldehyde solution (GA; Grade I; 25% H_2O), *N*-methyl-2-pyrrolidone (NMP) and acetic acid (glacial; ACS reagent; ≥99.7%) were purchased from Sigma–Aldrich (USA). Ethanol (extra pure grade) was obtained from Daejung Co. (South Korea). All aqueous solutions were prepared using purified water obtained from a double-distilled water system (Aquapuri 5, Korea).

Preparation & characterization of MSNC

To synthesize orange-colored nanoparticles of Mn-DTOGA for battery applications, we first dissolved 1.2 g (10 mmol) of DTO, 1.2 g of PVP, and 1.0 g of $Mn(OAc)_2$ in 150 mL of N_2-purged ethanol with the addition of a few drops of glacial acetic acid (~100 μL). The resulting mixture was refluxed with vigorous stirring for 1 h, during which time the solution turned red and reached its boiling point. Subsequently, a 25 % GA solution (4 mL, 10 mmol) was added to a Schlenk flask and allowed to react for 12 h. The resulting orange nanoparticles were obtained *via* filtration and centrifugation. The nanoparticles were then thoroughly washed with ethanol and dried overnight under vacuum at 40 °C.

High-resolution TEM and energy-dispersive X-ray spectroscopy (EDS) images were acquired using an ultra-corrected energy-filtered TEM microscope (Libra 200 HT MC Cs, Carl Zeiss, Germany) operating at an accelerating voltage of 200 kV. For the TEM analysis, a drop of a dilute solution of nanoparticles in ethanol was deposited onto ultrathin carbon-coated copper grids. The morphologies of the samples were characterized by field-emission SEM (S-4800, Hitachi, Japan) at the Korea Basic Science Institute, Daejeon. High-performance X-ray photoelectron spectroscopy (HP-XPS, VG Scientific ESCALAB 250) confirmed the chemical composition of the prepared samples (The Converging Materials Core Facility of Dong-Eui University, Busan and the Korea Basic Science Institute (KBSI), Busan.). Electrochemical measurements were performed using a potentiostat (VSP; Biological Science Instruments). The electrochemically active surface area (ECSA) was calculated based on the cyclic voltammograms recorded in a 1.0 M H_2SO_4 electrolyte saturated with N_2 at various scan rates.[24–26] The N_2 adsorption–desorption analysis was conducted using a volumetric nitrogen sorption system by ASAP2020 (Micromeritics, USA) in Korea Basic Science Institute (KBSI), Daejoen. The adsorption–desorption measurements were performed at liquid nitrogen temperature (77 K). The specific surface area (S_{BET}), the micropore volume (V_{mic}), and the external surface area were determined by means of a *t*-plot.[27] The total pore volume (V_{tot}) was calculated at relative pressure of $P/P_0 = 0.9889$. The pore sizes of the sample were analyzed using the Horvath–Kawazoe (H–K) method (microporosity)[28] and the Barret–Joyner–Halenda model (BJH) method (mesoporosity).[29]

Cell assembly and electrochemical testing

CV was conducted in the range of 0.05–2.0 V at the scan rate of 0.05 m V s^{-1}, and EIS measurements were performed from 1 MHz to 0.1 Hz using the potentiostat.[30]

To prepare the anode, a slurry was formed by mixing the MSNC powder, super-P, and polyvinylidene fluoride (weight content of 8 : 1 : 1) in NMP. The slurry was gently cast on Cu foil using a doctor's blade. The resulting anode films were dried at 90 °C for 10 h under vacuum.[31,32] Other materials, such as MnS, MnO, and hard carbon materials, were also carried out in the same manner as above.

CR-2032 cells (Li metal/MSNC, MnS, MnO, and hard carbon) were assembled in an argon-filled glove box with oxygen and moisture levels of less than 0.1 ppm. Commercial 1.0 M $LiPF_6$ in EC:DEC (1 : 1 vol) (5.0 wt% FEC) electrolyte and Celgard® separator were used for discharge–charge cycling studies.

Result and discussion

Concept and fabrication of MSNC nanoparticles

To synthesize the MSNC nanoparticles, we first prepared a precursor polymer, Mn-DTOGA. This polymer was synthesized

via condensation of two ligands, DTO and GA, in the presence of Mn(II) acetate ($Mn(OAc)_2$). This reaction results in the formation of imine bonds and polymerization of the Mn-DTOGA complex, which contains an acetate counter and Mn^{2+} ions.[23] The obtained coordination polymer was subjected to heat treatment at 1000 °C to obtain the final anode material for the LIBs (Fig. 1a). The degree of crystallinity of the materials was investigated using wide-angle XRD. The XRD pattern of the MSNC nanoparticles is shown in Fig. 1b, exhibiting multiple peaks corresponding to the (111), (002), (022), (113), (222), (004), and (024) crystal planes, demonstrating a cubic structure (ref: 98-008-9673).

XPS was used to determine the chemical composition of the MSNC nanoparticles. Fig. S1 (ESI†) shows the XPS spectrum of the MSNC, which reveals the presence of C, O, N, S, and Mn. The high-resolution C 1s XPS spectrum displays peaks corresponding to the C–C, C–O/C–N/C–S, and C═O bonds (Fig. 1c). The N 1s spectrum (Fig. 1d) confirms the presence of pyrrolic-N, quaternary-N, and pyridinic-N bonds in the material. The high-resolution O 1s XPS spectrum revealed the presence of metal–O, C–O, and C═O bonds (Fig. 1e). The S 2p spectrum (deconvoluted in Fig. 1f) exhibits peaks corresponding to C–S–C, MnS, and sulfate. The Mn 2p spectrum was deconvoluted into Mn^{2+} (MnO and MnS), $Mn^{3+,4+}$, and Mn^{2+} satellite peaks (Fig. 1g). The Mn 3s region was used to examine the oxidation state of Mn. The interval between the Mn $3S_{1/2}$ and Mn $3S_{3/2}$ peaks varied depending on the oxidation state of the Mn species. In this case, the appearance of two peaks in the Mn 3s spectrum (Fig. 1h) indicates the coupling of electrons between Mn 3s and Mn 3d. The shift in the binding energy of the Mn 3s peaks indicated a change in the oxidation state of Mn. The presence of a 5.9 eV interval in the spectrum corresponds to the Mn^{2+} state, suggesting the existence of MnO bonds.[33,34] All peak positions in the XPS spectra are listed in Table S1 (ESI†).

Microstructure characterization of MSNC nanoparticles

The morphologies and shapes of the prepared materials were confirmed using field-emission SEM. Fig. 2a shows the SEM images captured using different modes (secondary electrons and backscattered electrons). The average diameter of the MSNC nanoparticles is estimated to be approximately 300 nm, and they exhibited a spherical shape with a core–shell structure. Notably, the prepared nanoparticles exhibited a relatively narrow size distribution (Fig. S2, ESI†). To further elucidate the cluster morphology, TEM analysis was performed (Fig. 2b). The existence of core–shell formations with amorphous shells was confirmed by bright-field images. According to the EDS mapping data, the MnS core was located internally, whereas the carbon shell was located externally (Fig. 2c). Additionally, the line profile used to investigate the presence of particles in the core–shell configuration or individual dispersions shows a distinctive core–shell line profile. In this profile, the Mn and S peaks appear as island-shaped features at the center, whereas the carbon peak appears as a crater-shaped feature (Fig. S3, ESI†). As can be seen in Fig. S4 (ESI†), the Raman spectrum shows

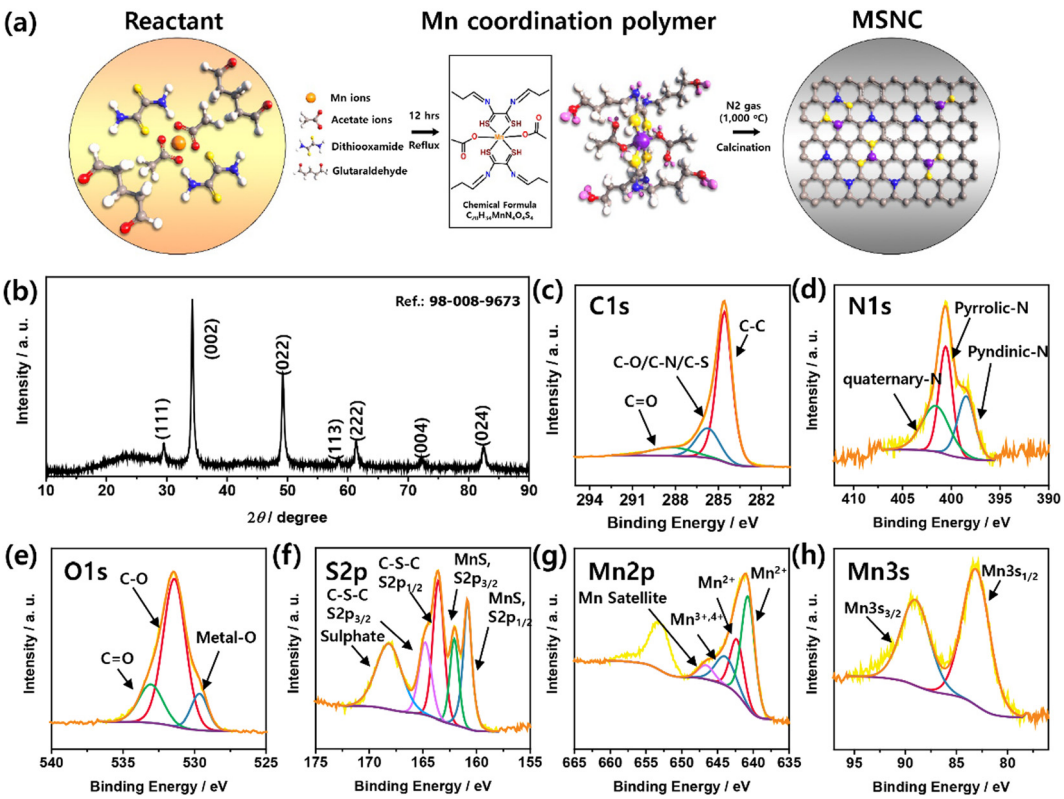

Fig. 1 (a) Schematic of the preparation of the MSNC material; (b) XRD measurement of MSNC; XPS spectra of MSNC: (c) C 1s, (d) N 1s, (e) O 1s, (f) S 2p, (g) Mn 2p, and (h) Mn 3s.

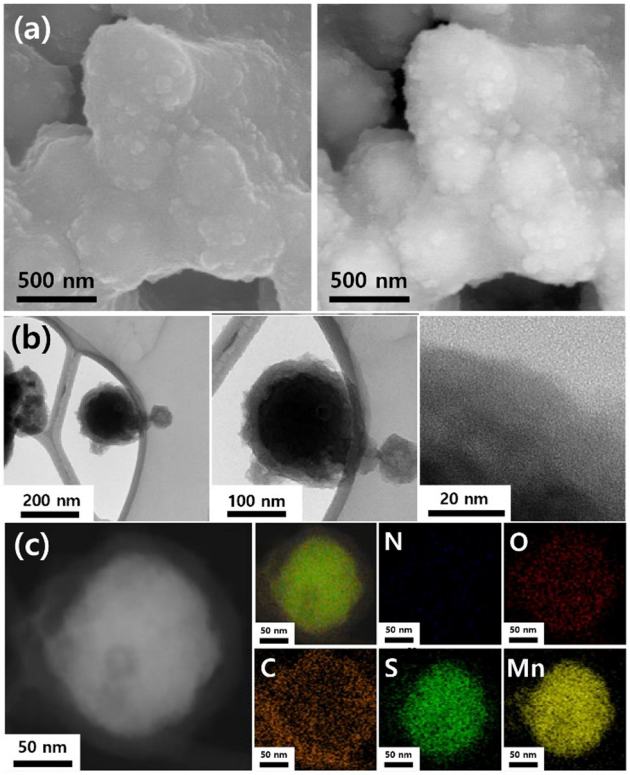

Fig. 2 (a) SEM (SE and BE modes), (b) high-resolution TEM, and (c) mapping images of MSNC (N, O, C, S, and Mn).

characteristic D and G bands at 1345.96 and 1579.34 cm^{-1}, respectively, typical for the disordered structure of hard carbon. Additionally, the N_2 adsorption–desorption isotherms of MSNC was revealed in Fig. S5a (ESI†). The pore size distribution was calculated using the BJH method (Fig. S5b, ESI†) and the H–K method (Fig. S5c, ESI†). The pore structure of the prepared material, as determined using the BET method, only provided 4.64 $m^2\ g^{-1}$.

To confirm the active area, the ECSA in a 1 M H_2SO_4 solution was measured, as shown in Fig. S6 (ESI†). The active surface area of the MSNC electrode is calculated using the double-layer capacitance, ECSA = C_{dl}/C_s, where C_{dl} represents the double-layer capacitance and C_s (0.029 mF cm^{-2}) represents the specific capacitance of the sample. The surface area of the MSNC electrode was 0.242 cm^2.

Electrochemical characterization and fundamental consideration of the MSNC electrode

Fig. 3a shows the CV curves of the MSNC-based electrode evaluated at a scan rate of 0.5 mV s^{-1} and a potential window of 0.05–2.0 V during the first five cycles. In the first cathodic scan, the distinct peak at approximately 0.25 V was attributed to the reduction of MnS/MnO to metallic Mn and Li–O, and Li–S complex, in addition of the generation of a solid-electrolyte interphase (SEI) layer.[26] In the following anodic sweep, the feature at approximately 1.25 V was ascribed to the reconversion of Mn into metal oxides and sulfide species.[20,22,35] In addition, the EIS spectra of the MSNC electrode before and after five cycles are shown in Fig. 3b. The impedance spectra before and after 5th cycles were analyzed using a Randles equivalent circuit. The half of the bulk resistance (R_b) values for before and after 5th cycles are determined to be 1.943 and 2.551 Ω, respectively. The surface layer resistance (R_{sl}) values before and after 5th cycles were determined to be 417.4 and 7.695 Ω, respectively. There is a big difference in the surface layer resistance before and after the cycle. The reason seems to be the difference according to the formation of the SEI layer. After five cycles, the semicircle representing the charge transfer resistance (R_{ct}) in the high-frequency range (37.42 Ω) is approximately 2.2 times smaller than that of the initial value (89.69 Ω). This indicates that the electrochemical activation and cycling processes enhanced the speed of electronic transfer and interfacial electrochemical reactions.[36,37]

Fig. 3c–e illustrates the discharge/charge curves of the MSNC electrode over 500 cycles at a rate of 0.2 C, ranging from 0.05 to 2.0 V. The MSNC electrode initially exhibits discharge and charge capacities of 598 and 293 mA h g^{-1}, respectively (Fig. S7, ESI†), which was confirmed similar to profiles of MnS and MnO cells. Further information was described in the ESI.† (Fig. S8, ESI†). The decrease in capacity was attributed to the irreversible formation of SEI layers and electrolyte decomposition in the low-potential regions. Furthermore, the presence of a plateau at approximately 0.63 V in the discharge curves is attributed to the formation of an Mn and Li sulfide/oxide matrix. During the initial charging process, the plateau at approximately 1.2 V was associated with Mn sulfidation/oxidation.[22,35]

Region 1 (2.0–0.01 V)

$$MnS/MnO + 2Li^+ + 2e^- \rightarrow Mn^0 + Li_2S/Li_2O \quad (1)$$

Region 2 (0.01–2.0 V)

$$Mn^0 + Li_2S/Li_2O \rightarrow MnS/MnO + 2Li^+ + 2e^- \quad (2)$$

Further discharge/charge profiles explain the reversible capacities at approximately 232 mA h g^{-1} with 100% coulombic efficiency for 500 cycles. Although the electrochemical performance of MSNC needs to be improved in terms of capacity and irreversibility, this result indicates a superior cycle performance compared to that of commercial HC (hard carbon) in Fig. S9 and 10 (ESI†) (HC-pac-2m, Aekyung Chemical Co., Ltd.). Fig. 3e shows the rate capability of the MSNC as an anode material, which was assessed to further determine its applicability. The capacity values provided by MSNC at various rates of 0.05, 0.1, 0.2, 0.5, 1.0, and 2.0 C are 359, 317, 273, 221, 183, and 145 mA h g^{-1}, respectively. After 24 cycles, when the C-rate is reduced to 0.05C, the capacity returns to 332 mA h g^{-1}. We compared electrochemical performances of recently reported MnS and/or MnO-based carbon composites anodes. As shown in Table S2 (ESI†), MSNC anodes (in this work) exhibit superior cyclic stability with capacity retention of 79% after the 500th cycle, and lower voltage operation as anode. However, the anodes presented relatively low initial charge capacity, which might be due to their low contents of Mn-based active materials and relatively narrow voltage cut-off range. Capacity values provided by MSNC at various rates of 0.05, 0.1, 0.2, 0.5, 1.0, and 2.0 C are 359, 317, 273, 221, 183, and 145 mA h g^{-1}.

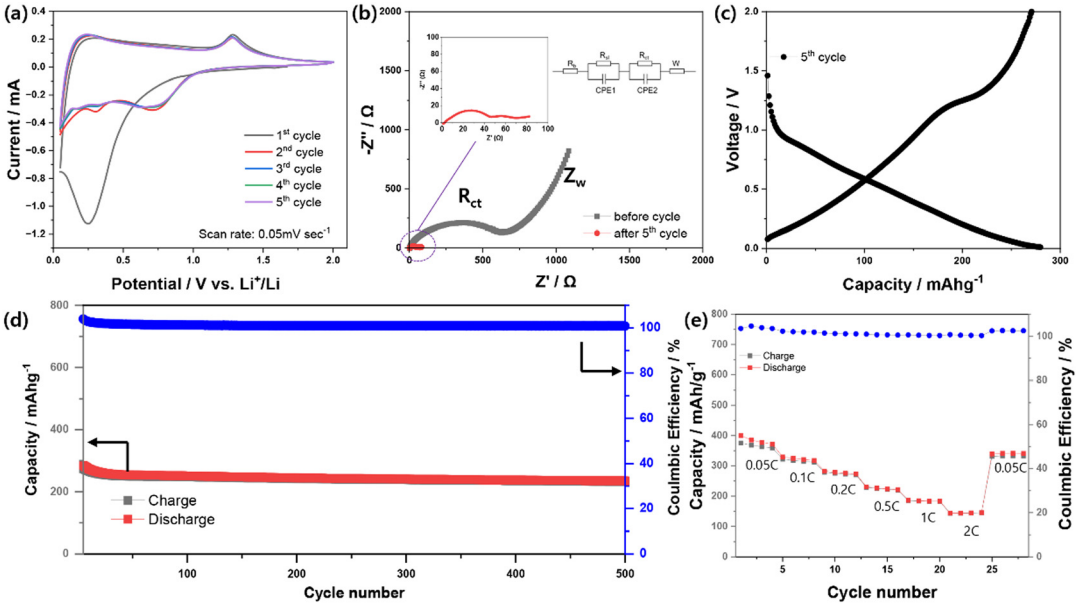

Fig. 3 (a) Cyclic voltammetry and (b) EIS characteristics of MSNC (Li/MSNC cell). (c) Discharge/charge profiles, (d) cyclability test cycled between 0.05 and 2 V *versus* Li^+/Li with 0.2C, and (e) C-rate test from 0.05C to 2C.

In situ XRD measurements were performed during the first cycle of the discharge/charge process to gain further insight into the Li storage mechanism of the MSNC material (Fig. S11, ESI†). The evolution of the XRD patterns (30 scans) and the corresponding discharge/charge profiles are shown in Fig. 4a. The intensities at 34.5° and 49.5° of MnS decreased during the first charging cycle. From this result, we could confirm that the MnS complex is reduced to metallic Mn during the first discharge, followed by the formation of the MnS/MnO complex, as mentioned above, during the subsequent charging process. The color-coded images (Fig. 4b) obtained from additional scans (144 scans over three cycles) provide evidence that the MnS complex is also reduced as the cycling progresses, which is considered to be attributed to SEI formation during cycling.

XPS spectra were obtained to determine the chemical composition of the MSNC after one and 20 cycles. The spectra show the presence of C, N, O, S, P, Li, F, and Mn in the prepared electrodes (Fig. S12, ESI†). Fig. 4c–j shows the high-resolution spectra of S 2p, Mn 2p, O 1s, and Li 1s (1 and 20 cycles), and all the peak positions of the XPS are listed in Table S3 and S4 (ESI†). Fig. S13 (ESI†) shows the C 1s spectra after cycles one and 20 cycles, which reveal the presence of C–C, C–O/C–N/C–S, C═O, and C–F bonds. In the C 1s spectra, C–F bonds were newly introduced compared to the powder sample, which was due to $LiPF_6$ from the electrolyte. The high-resolution S 2p XPS spectrum displays peaks corresponding to MnS, C–S–C, and sulfate (Fig. 4c and g). The intensity of the sulfate bond peak decreased in the sample after 20 cycles compared with that after only one cycle. This is because O ions emerge from the broken S–O bonds during cycling. Furthermore, the intensity of the MnS peak increased in the sample after 20 cycles compared to that of the sample after only one cycle. In the Mn 2p region (Fig. 4d and h), Mn^{2+} (MnS and MnO), $Mn^{3+,4+}$, and Mn^{2+} satellite peaks were observed. Interestingly, as shown in the Mn 2s spectra, the peak intensity of MnO decreased relative to that of MnS after 20 cycles, suggesting that MnO was primarily involved in the cycling reaction. The O 1s XPS spectra (after one and 20 cycles) were deconvoluted into peaks corresponding to Li_2O, MnO, and C═O groups (Fig. 4e, i). From the O 1s spectra, it can be observed that the peak intensity of Li_2O is enhanced in comparison to that of MnO after 20 cycles. Based on this result, we propose that O ions are released during the decomposition of the predominant MnO bond with Li ions during cycling. Fig. 4f and j show the XPS profiles of the high-resolution Li 1s peaks corresponding to LiF and Li_2O, respectively. Compared to that after one cycle, the Li_2O peak intensity after 20 cycles increased, thereby the Li 1s peak results support the previous results for the O 1s peak.

Therefore, the *in situ* XRD and XPS data validate the roles of MnS and MnO during the charge/discharge process. Furthermore, MnO decomposed into Mn and O ions with formation of Mn–O and Li–O, as observed in the O 1s and Li 1s spectra. In particular, the amount of O1 decreased with depth after 1 and 20 cycles, the amount of S1 was slightly reduced as shown in XPS depth study (Fig. S14, ESI†). This indicates that, as mentioned previously, MnO undergoes reduction, contributing to the enhanced capacity during the cycle reaction. Likewise, MnS partly contributed to the redox reaction. These findings demonstrate that MnS/MnO plays a crucial role in the charging and discharging processes for a stable long cycles.

Conclusions

We successfully synthesized MSNC nanoparticles from a novel Mn^{2+}-coordinated polymer (Mn-DTOGA). MSNC nanoparticles were prepared by optimizing the calcination temperature to 1000 °C. The physical and chemical characteristics of the MSNC

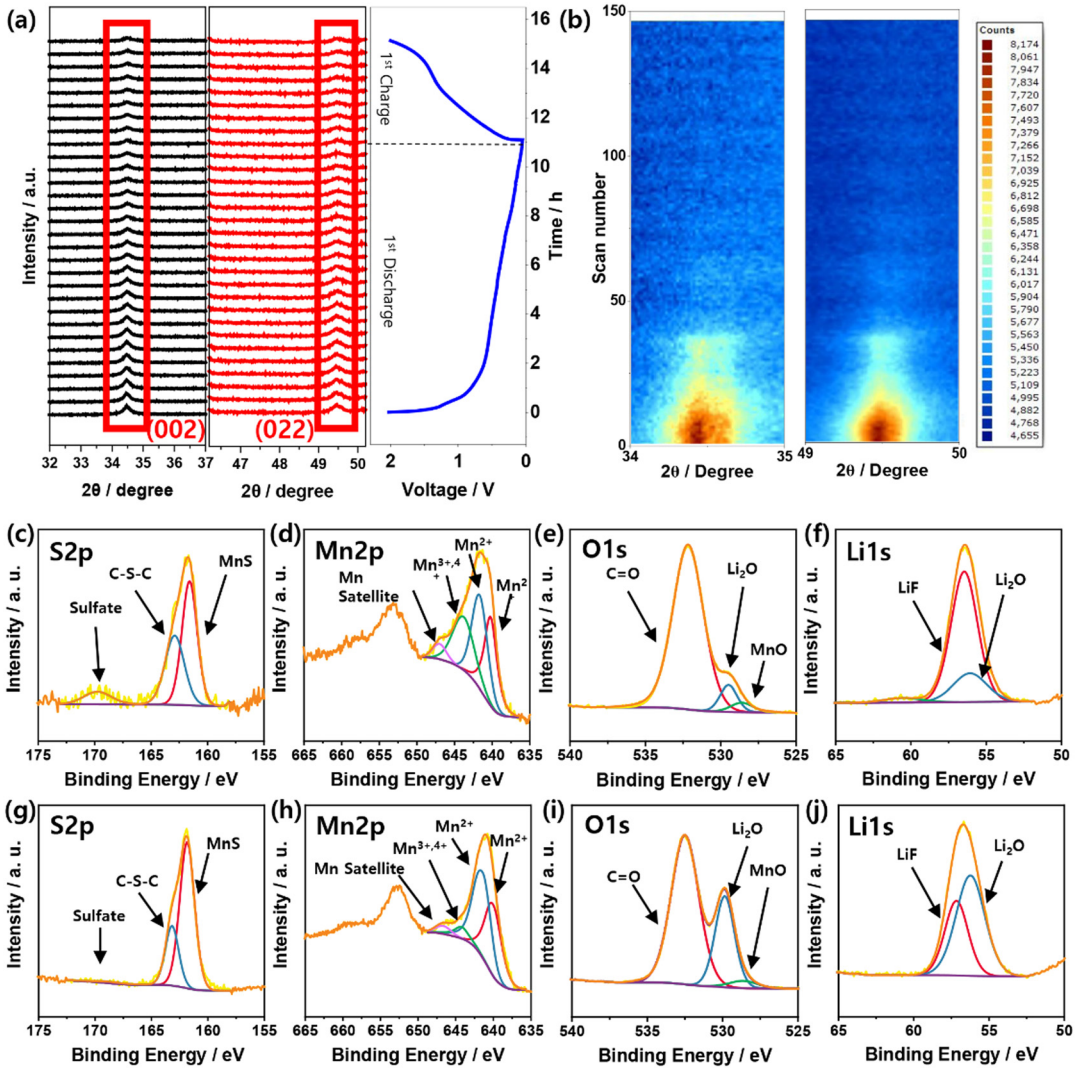

Fig. 4 (a) *In situ* XRD measurement of Li/MSNC cell during discharge/charge, (b) MSNC, and XPS spectra of MSNC electrode after 1 cycle (c)–(f), 20 cycles (g)–(j).

were verified using XPS, XRD, SEM, and TEM which demonstrated the facile synthesis, exceptional controllability, and uniformity of the material. To evaluate the electrochemical properties of MSNC as a potential anode material for LIBs, a comprehensive analysis was conducted using CV, EIS, and galvanostatic charge–discharge tests. The findings revealed the remarkable cycling stability of the material with enhanced electrochemical activation, as it displayed superior performance of over 230 mA h g^{-1} for 500 cycles at a rate of 0.2 C. Moreover, *in situ* XRD and XPS analyses were performed, which confirmed the reduction of the MnS/MnO complex to metallic Mn and Li_2S/Li_2O with SEI formation during discharge and reconversion of metallic Mn to the MnS/MnO complex during charging. Our findings offer compelling evidence for the immense potential of MSNC nanoparticles in advancing the field of high-energy-density LIBs owing to their exceptional chemical, physical, and electrochemical characteristics with superior controllability. For high-energy-density batteries, further research will be conducted to improve the irreversibility in the initial cycle and to explore strategies for increasing the capacity by adopting transition metals (*e.g.*, Ni, Co, and Zn) for advanced Li and Na (K)-and Na-ion batteries.

Author contributions

We strongly encourage authors to include author contributions and recommend using CRediT for standardized contribution descriptions. Please refer to our general author guidelines for more information about authorship.

Conflicts of interest

There are no conflicts to declare.

Acknowledgements

We are grateful for financial support from the Basic Science Research Program through the National Research Foundation

of Korea (NRF) funded by the Ministry of Education (RS-2023-00247162) and the Commercialization Promotion Agency for R&D Outcomes (COMPA) grant funded by the Korean Government (Ministry of Science and ICT) (RS-2023-00304768).

Notes and references

1 J. Park, H. Jin, S. Yeon, H. W. Kim and M. Ko, Oxide-Based Pseudo-Solid-State Hybrid Electrolyte Functionalized by Ionic Liquid for Lithium Metal Batteries, *Energy Technol.*, 2022, **11**, 2201153.

2 H. W. Kim, J. Han, Y. J. Lim, Y. Choi, E. Lee and Y. Kim, 3D Ion-Conducting, Scalable, and Mechanically Reinforced Ceramic Film for High Voltage Solid-State Batteries, *Adv. Funct. Mater.*, 2021, **31**, 2002008.

3 R. Hausbrand, G. Cherkashinin, H. Ehrenberg, G. Groting, K. Albe, C. Hess and W. Jaegermann, Fundamental degradation mechanisms of layered oxide Li-ion battery cathode materials: Methodology, insights and novel approaches, *Mater. Sci. Eng. B*, 2015, **192**, 3–25.

4 H. W. Kim, H.-J. Kim, H. Byepn, J. Kim, J. W. Yang, Y. Kim and J. K. Kim, Binder-free organic cathode based on nitroxide radical polymer-functionalized carbon nanotubes and gel polymer electrolyte for high-performance sodium organic polymer batteries, *J. Mater. Chem. A*, 2020, **8**, 17980–17986.

5 Y. J. Lim, J. Han, H. W. Kim, Y. Choi, E. Lee and Y. Kim, An epoxy-reinforced ceramic sheet as a durable solid electrolyte for solid state Na-ion batteries, *J. Mater. Chem. A*, 2020, **8**, 14528–14537.

6 J. B. Goodenough and Y. Kim, Challenges for rechargeable Li batteries, *Chem. Mater.*, 2010, **22**, 587–603.

7 M. Ko, S. Chae, J. Ma, N. Kim, H.-W. Lee, Y. Cui and J. Cho, Scalable synthesis of silicon-nanolayer-embedded graphite for high-energy lithium-ion batteries, *Nat. Energy*, 2016, **1**, 16113.

8 J. Sung, N. Kim, J. Ma, J. H. Lee, S. H. Joo, T. Lee, S. Chae, M. Yoon, Y. Lee, J. Hwang, S. K. Kwak and J. Cho, Subnanosized silicon anode via crystal growth inhibition mechanism and its application in a prototype battery pack, *Nat. Energy*, 2021, **6**, 1164–1175.

9 Y.-J. Li, C.-Y. Fan, H.-H. Li, K.-C. Huang, J.-P. Zhang and X.-L. Wu, 3D Hierarchical Microballs Constructed by Intertwined MnO@N-doped Carbon Nanofibers towards Superior Lithium-Storage Properties, *Chem. – Eur. J.*, 2018, **24**, 9606–9611.

10 Y. Ma, Y. Ma, D. Geiger, U. Kaiser, H. Zhang, G.-T. Kim, T. Diemant, R. J. Behm, A. Varzi and S. Passerini, ZnO/$ZnFe_2O_4$/N-doped C micro-polyhedrons with hierarchical hollow structure as high-performance anodes for lithium-ion batteries, *Nano Energy*, 2017, **42**, 341–352.

11 Y. Ji, Y. Ma, R. Liu, Y. Ma, K. Cao, U. Kaiser, A. Varzi, Y.-F. Song, S. Passerini and C. Streb, Modular development of metal oxide/carbon composites for electrochemical energy conversion and storage, *J. Mater. Chem. A*, 2019, **7**, 13096–13102.

12 S. Wu, F. Xu, Y. Li, C. Liu, Y. Zhang and H. Fan, Synergistically enhanced sodium ion storage from encapsulating highly dispersed cobalt nanodots into N, P, S tri-doped hexapod carbon framework, *J. Colloid Interface Sci.*, 2023, **649**, 741–749.

13 X.-T. Wang, Y. Yang, J.-Z. Guo, Z.-Y. Gu, E. H. Ang, Z.-H. Sun, W.-H. Li, H.-J. Liang and X.-L. Wu, An advanced cathode composite for co-utilization of cations and anions in lithium batteries, *J. Mater. Sci. Technol.*, 2022, **102**, 72–79.

14 J.-M. Cao, I. V. Zatovsky, Z.-Y. Gu, J.-L. Yang, X.-X. Zhao, J.-Z. Guo, H. Xu and X.-L. Wu, Two-dimensional MXene with multidimensional carbonaceous matrix: A platform for general-purpose functional materials, *Prog. Mater. Sci.*, 2023, **135**, 101105.

15 Y. Ma, Y. Ma, T. Diemant, K. Cao, U. Kaiser, R. J. Behm, A. Varzi and S. Passerini, Embedding Heterostructured α-MnS/MnO Nanoparticles in S-Doped Carbonaceous Porous Framework as High-Performance Anode for Lithium-Ion Batteries, *ChemElectroChem*, 2021, **8**, 918–927.

16 Q.-M. Yin, Z.-Y. Gu, Y. Liu, H.-Y. Lü, Y.-T. Liu, Y.-N. Liu, M.-Y. Su, J.-Z. Guo and X.-L. Wu, Mn-Rich Phosphate Cathode for Sodium-Ion Batteries: Anion-Regulated Solid Solution Behavior and Long-Term Cycle Life, *Adv. Funct. Mater.*, 2023, **33**, 2304046.

17 D. Xu, R. Jiao, Y. Sun, D. Sun, X. Zhang, S. Zeng and Y. Di, L-Cysteine-Assisted Synthesis of Urchin-Like γ-MnS and Its Lithium Storage Properties, *Nanoscale Res. Lett.*, 2016, **11**, 444.

18 J. Ning, D. Zhang, H. Song, X. Chen and J. Zhou, Branched carbon-encapsulated MnS core/shell nanochains prepared via oriented attachment for lithium-ion storage, *J. Mater. Chem. A*, 2016, **4**, 12098–12105.

19 G. Zhu, L. Wang, H. Lin, L. Ma, P. Zhao, Y. Hu, T. Chen, R. Chen, Y. Wang, Z. Tie, J. Liu and Z. Jin, Walnut-Like Multicore–Shell MnO Encapsulated Nitrogen-Rich Carbon Nanocapsules as Anode Material for Long-Cycling and Soft-Packed Lithium-Ion Batteries, *Adv. Funct. Mater.*, 2018, **28**, 1800003.

20 Y. Wang, H. Wu, L. Huang, H. Zhao, Z. Liu, X. Chen, H. Liu and Y. Zhang, Hierarchically Porous N, S co-doped Carbon-Embedded Dual Phase MnO/MnS Nanoparticles for Efficient Lithium-Ion Storage, *Inorg. Chem.*, 2018, **57**, 7993–8001.

21 X. Yi, W. He, X. Zhang, G. Yang and Y. Wang, Hollow mesoporous MnO/MnS/SiC/S-CN composites prepared from soda pulping black liquor for lithium-ion batteries, *J. Alloys Compd.*, 2018, **735**, 1306–1313.

22 K. Wang, K. Zhao, Y. Wang, H. Li, H. Jiang and L. Chen, N, S co-doped carbon confined MnO/MnS heterostructures derived from a one-step pyrolysis of Mn-methionine frameworks for advanced lithium storage, *J. Alloys Compd.*, 2021, **860**, 158451.

23 K. Shim, K.-D. Seo and H. J. Kim, Synthesis of MnS/MnO Decorated N,S-Doped Carbon Derived from a Mn(II)-Coordinated Polymer for the Catalytic Oxidation of H_2O_2 and Bisphenol A, *Adv. Funct. Mater.*, 2023, **33**, 2210549.

24 F. Luo, R. Xu, S. Ma, Q. Zhang, H. Hu, K. Qu, S. Xiao, Z. Yang and W. Cai, Engineering oxygen vacancies of cobalt

tungstate nanoparticles enable efficient water splitting in alkaline medium, *Appl. Catal., B*, 2019, **259**, 118090.

25 Y. Yan, A. Li, C. Lu, T. Zhai, S. Lu, W. Li and W. Zhou, Double-layered yolk-shell microspheres with $NiCo_2S_4$-Ni_9S_8-C hetero-interfaces as advanced battery-type electrode for hybrid supercapacitors, *Chem. Eng. J.*, 2020, **396**, 125316.

26 Z. Sadighi, J. Liu, L. Zhao, F. Ciucci and J.-K. Kim, Metallic MoS_2 nanosheets: multifunctional electrocatalyst for the ORR, OER and Li–O_2 batteries, *Nanoscale*, 2018, **10**, 22549–22559.

27 S. Lowell and J. E. Shields, *Powder Surface area and porosity*, Chapman & Hall, London, 3rd edn, 1991, pp. 77–84.

28 G. Horvath and K. Kawazoe, Method for the calculation of effective pore size distribution in molecular sieve carbon, *J. Chem. Eng. Jpn.*, 1983, **16**, 470.

29 E. P. Barrett, L. G. Joyner and P. P. Halenda, The determination of pore volume and area distributions in porous substances. I. Computations from Nitrogen Isotherms, *J. Am. Chem. Soc.*, 1951, **73**, 373–380.

30 M. Palanisamy, H. W. Kim, S. Heo, E. Lee and Y. Kim, Insights into the Dual-Electrode Characteristics of Layered $Na_{0.5}Ni_{0.25}Mn_{0.75}O_2$ Materials for Sodium-Ion Batteries, *ACS Appl. Mater. Interfaces*, 2017, **9**, 10618–10625.

31 K. W. Kim, H. W. Kim, Y. Kim and J. K. Kim, Composite gel polymer electrolyte with ceramic particles for $LiNi_{1/3}Mn_{1/3}Co_{1/3}O_2$-$Li_4Ti_5O_{12}$ lithium-ion batteries, *Electrochim. Acta*, 2017, **236**, 394–398.

32 H. W. Kim, M. Palanisamy, Y. J. Lim, J. H. Kim, S. C. Nam and Y. Kim, Hybrid solid electrolyte with the combination of $Li_7La_3Zr_2O_{12}$ ceramic and ionic liquid for high voltage pseudo-solid-state Li-ion batteries, *J. Mater. Chem. A*, 2016, **4**, 17025–17032.

33 J. L. Junta and M. F. Hochella. Jr., Manganese (II) oxidation at mineral surfaces: A microscopic and spectroscopic study, *Geochim. Cosmochim. Acta*, 1994, **58**, 4985–4999.

34 A. J. Nelson, J. G. Reynolds and J. W. Roos, Core-level satellites and outer core-level multiplet splitting in Mn model compounds, *J. Vac. Sci. Technol. A*, 2000, **18**, 1072–1076.

35 Q. Han, W. Zhang, Z. Han, F. Wang, D. Geng, X. Li, Y. Li and X. Zhang, Preparation of PAN-based carbon fiber@MnO_2 composite as an anode material for structural lithium-ion batteries, *J. Mater. Sci.*, 2019, **54**, 11972–11982.

36 Y. Liu, Y. Qiao, W.-X. Zhang, Z. Li, X.-L. Hu, L.-X. Yuan and Y.-H. Huang, Coral-like α-MnS composites with N-doped carbon as anode materials for high-performance lithium-ion batteries, *J. Mater. Chem.*, 2012, **22**, 24026–24033.

37 S. S. Lee, Y. J. Lim, H. W. Kim, J. K. Kim, Y. G. Jung and Y. Kim, Electrochemical properties of a ceramic-polymer-composite-solid electrolyte for Li-ion batteries, *Solid State Ion.*, 2016, **284**, 20–24.